Resonant Inelastic X-ray Scattering Measurement and Simulation to Understand Promoter Effects in Platinum Catalysts

Brandon C. Bukowski‡, Stephen C. Purdy‡, Evan C. Wegener, Zhenwei Wu, A. Jeremy Kropf, Guanghui Zhang, Jeffrey T. Miller*, Jeffrey Greeley*

Charles D. Davidson School of Chemical Engineering, Purdue University, 480 Stadium Mall Drive, West Lafayette Indiana 47907, United States

Chemical Sciences and Engineering Division, Argonne National Laboratory, 9700 South Cass Avenue, Argonne, Illinois 60439, United States

State Key Laboratory of Fine Chemicals, PSU-DUT Joint Center for Energy Research, School of Chemical Engineering, Dalian University of Technology, Dalian, Liaoning 116024, PR China

Supplementary Information

S.1 Supplementary methods

S.1.1 Catalyst Synthesis

Bimetallic Pt-Ga catalysts were synthesized by sequential incipient wetness impregnation with a target loading of 5% Pt and 2.5% Ga. 1.25 g of 10 wt% $Ga(NO_3)_3$ solution and 1.33 g of Citric acid was dissolved in Millipore water and diluted to a solution volume of 5 ml and pH adjusted to 11 though the addition of 30% ammonium hydroxide. The solution was added dropwise to 5.00 g of Davasil 646 SiO_2. The Ga-SiO_2 was then dried at 125°C overnight and then calcined under flowing air at 600°C for 3 hours. 0.166 g of $Pt(NH_3)_4(NO_3)_2$ was dissolved in 1 mL of Millipore water and diluted to a total volume of 5 mL. The solution was pH adjusted to 11 with 30% ammonium hydroxide and added dropwise to the calcined Ga-SiO_2. The catalyst was dried at 125°C overnight and calcined at 350°C for 3 hours. The Pt-Ga catalyst was then reduced at 200C in 5% H_2 (balance N_2) at 100 ccm for 30 minutes and then 600°C in the same gas for 30 minutes. The catalyst was then cooled to room temperature in N_2 and passivated in air. A monometallic 3% Pt on SiO2 catalyst was synthesized in the same manner with the Pt loading adjusted by decreasing the mass of $Pt(NH_3)_4(NO_3)_2$ used during platinum impregnation.

S.1.2 Scanning Transmission Electron Microscopy (STEM)

The particle size of the reduced catalyst was measured by STEM imaging. STEM images were collected on an FEI Titan operated in STEM mode using an accelerating voltage of 300 keV and a high angle annular dark field (HAADF) detector. Samples for STEM were dispersed in isopropyl alcohol and dropped onto an ultrathin carbon film Au TEM grid (TedPella) and subsequently dried on a hotplate at 80°C. Image processing was performed using the FIJI distribution of ImageJ software, with a minimum of 100 particles measured to give the particle size distribution[1].

S.1.3 In-Situ X-ray Absorption Spectroscopy (XAS)

In-Situ XAS at the Pt L_3 edge (11562.76 eV) was performed at the MRCAT bending magnet line (10BM) of the advanced photon source. Samples were measured in transmission mode using a set of 3 ion chambers, which allowed for simultaneous measurement of the sample and a reference foil. Samples for XAS were ground in a mortar and pestle and pressed into a stainless steel sample holder. Samples were treated in a quartz tube reactor with Kapton windows and valves for gas flow. Catalysts were pretreated at 550°C for 30 minutes in 3.5% H_2. The reactor was then purged at temperature for 5 minutes with UHP Helium which was further purified using a Restek oxygen and water trap before cooling to room temperature in the same gas. The reactor atmosphere was then isolated using 3-way ball valves and transferred to the beamline for analysis.

XAS data analysis was performed using WinXAS software. Experimental phase and amplitude functions for Pt-Pt scattering was extracted from Pt foil (12 neighbors, 2.77 Å). Phase and amplitude functions for Pt-Ga scattering was generated using FEFF6 with a bond distance of 2.75 Å using the amplitude reduction factor (0.79) and Debye-Waller factor (0.004 Å^2) fit for the platinum foil. EXAFS data was k^2 weighted and Fourier transformed over k range of 2.6-12 Å^{-1} and the first shell scattering was isolated over an R range of 1.5-3.25 Å. Fitting was performed over the R range of the first shell isolation using a least squares approach allowing the coordination number, bond distance and Debye-Waller factor to vary.

S.1.4 In-Situ Synchrotron X-ray Diffraction (XRD)

In-Situ synchrotron X-ray diffraction measurements were performed at the 11ID-C beamline at the advanced photon source. Data was acquired in transmission mode using an X-ray wavelength of 0.117418 Å (105.091 keV) and a Perkin-Elmer large area detector. Detector calibration was

performed using a CeO_2 standard. Samples were pressed into a thin pellet and loaded into a Linkam Thermal Stage, which allowed reactant gas flow during in-situ XRD measurement. The cell was purged with He for 5 minutes before flowing 100 ccm of 3.5% H_2 (balance He) and ramping the cell temperature to 600°C for 20 minutes. Diffraction patterns were collected at high temperature and the sample was then cooled to 35°C under gas flow and diffraction patterns were collected again. The SiO_2 support and empty cell were treated by the same procedure and scanned for background subtraction. 2D diffraction patterns were integrated using Fit2D software, giving standard powder patterns[2,3]. Diffraction patterns of Pt-Ga phases were simulated using MAUD using reference CIF files from ICSD[4].

S.1.5 X-ray Photoelectron Spectroscopy

XPS measurements were made on a Kratos Axis Ultra Imaging DLD spectrometer. Before measurement, the catalysts were treated in a catalytic cell (CatCell) attached to the spectrometer, which allowed for gas treatment and transfer to the spectrometer without exposing the catalysts to oxygen. Monochromated Al Kα (1486.69 eV) X-rays were used, and photoelectrons were measured using a hemispherical electron energy analyzer operated with a constant pass energy of 20 eV. Differential charging was mitigated using a built in Kratos charge neutralizer. Before measurement, catalyst samples were pretreated in 5% H_2 (balance Ar) for 30 minutes at 550°C; sample were then transferred under UHV to the analysis chamber for measurement. The base pressure of the CatCell and analysis chamber was $4x10^{-8}$ and $2x10^{-9}$ Torr respectively. Data analysis was performed using CasaXPS software. The binding energy scale was charge corrected using the Si 2p peak which was set to 103.7 eV. The Pt 4f photoemission peaks were fit using an asymmetric Lorentzian function (LF(a,b,c,d)) and a Shirley background. Fits of the Pt 4f 7/2 and 5/2 components were constrained to have the same full width at half maximum (FWHM) and the

peak area ratio for the two components was fixed at 0.75, the peak position, area and full width at half maximum were allowed to vary.

S.2 Supplementary discussion

S.2.1 Pt-Ga phase identification

Metal nanoparticle size was measured on catalysts after reduction at 550°C and subsequent exposure to air. The number average particle size for the 5Pt-2.5Ga catalyst was 1.8±0.5 nm. Figure S.3.1 shows the number average particle size distribution and a representative STEM image for 5Pt-2.5Ga. The metal particle size is comparable to all other Pt alloy catalysts measured in this study. The monometallic Pt catalyst had a particle size of 2.1±0.6 nm.

In-Situ XAS measurements at the Pt L_3 edge were performed to determine if a bimetallic formed. Figure 2a shows the X-ray absorption near edge structure (XANES) for a monometallic catalyst and the bimetallic 5Pt-2.5Ga catalyst. The edge energy of the Pt catalyst is 11562.76 eV, consistent with metallic platinum. The Pt-Ga catalyst has an edge energy shifted to 11563.3 eV and the white line is broadened, consistent with a change in the energy distribution of the unfilled 5d states resulting from alloy formation.

Figure S.3.2 shows the R space EXAFS spectra of 3Pt and 5Pt-2.5Ga. The monometallic Pt catalyst has 3 peaks typical of scattering from platinum neighbors. The first shell scattering envelope for the Pt-Ga catalyst changes relative to the monometallic Pt catalyst due the incorporation of Pt-Ga scattering. The Pt-Ga catalysts still has 3 peaks, but the position is shifted to lower R values and the relative intensity of each is modified relative to platinum: the first (low R) peak in the Pt-Ga catalyst is close to the same height as the middle peak, whereas the low R peak in the Pt spectra is

the lowest peak and the middle peak is the highest. Fitting the monometallic Pt catalyst gave a Pt-Pt coordination number of 8.8 at a bond distance of 2.74. Fitting the Pt-Ga catalyst gave a Pt-Pt coordination number of 4.9 at a distance of 2.74 Å angstroms and a Pt-Ga coordination of 1.7 at a bond distance of 2.48 Å.

The phase composition of the bimetallic Pt-Ga catalyst was determined by in-situ synchrotron XRD. Figure S.3.3 shows the powder XRD pattern for 5Pt-2.5Ga as well as simulated XRD patterns of Pt_3Ga. The experimental diffraction peaks are broad due to the small particle size. The 2 theta range over which the typical primary reflections occur is much smaller than in a laboratory XRD pattern due to the high X-ray energy used (105.091 keV). The 5Pt-2.5Ga catalyst show primary reflections typical of an FCC lattice. Four peaks are clearly resolved, (111), (200) (220) and (311), but in addition superlattice diffraction peaks are evident in the 5Pt-2.5Ga catalyst: (110), (210) and (211), which are indicative of an $L1_2$ ($AuCu_3$) structure. The presence of the superlattice diffraction peaks and FCC primary reflections are consistent with the Pt_3Ga intermetallic phase. Nevertheless, the experimental pattern does not match the simulation perfectly. Compared to the standard Pt_3Ga pattern, the peaks in the 5Pt-2.5Ga are shifted to lower angle (0.006° for the most intense peak). The (111) and (220) peak maxima have the least overlap by neighboring peaks and are used to calculated the lattice parameter. The peak position of the (111) and (220) peaks is 2.983° and 4.873° respectively, both giving a lattice parameter of 3.90 Å., which is larger than the 3.892 Å given by the Pt_3Ga standard, such a difference cannot be accounted for by a nanoparticle size effect, where the large fraction of undercoordinated surface atoms causes a decrease in the lattice parameter. A plausible explanation is microstrain caused by the presence of a thin shell layer of a second phase with a larger lattice parameter which cannot be resolved by synchrotron

XRD. This interpretation is consistent with the EXAFS results which show a local platinum environment which is platinum rich with respect to that expected for Pt_3Ga.

S.2.2 Spectrometer details

The bent crystal geometry of the spectrometer used in this study allows for the selective measurement of fluorescence from the $L\beta_5$ decay mode (L_3-$O_{4,5}$), which corresponds to a $5d_{3/2}$ or $5d_{5/2}$ electron filling the core hole. Below the absorption edge (11.56276 keV for Pt), the incident X-rays do not have enough energy to excite the $2p_{3/2}$ electron into an unfilled valence state and no fluorescence is detected. The onset of fluorescence from the $L\beta_5$ decay mode occurs near the absorption edge and manifests in the RIXS plots as a broad maximum with an energy transfer value greater than zero. For platinum, the inelastic peak maximum occurs at an energy transfer value of 2.8 eV. Because the $L\beta_5$ probes all filled 5d states, and the L_3 edge probes all unfilled 5d states, the energy transfer maximum represents the energy separation between the weighted average energy of the filled 5d states and the weighted average energy of the unfilled 5d states. The broadness of the inelastic scattering peak reflects the width of the d band in platinum and platinum alloys convoluted with the resolution function of the spectrometer and lifetime broadening.

S.2.3 XPS core level shifts

Table S.3.4 shows the Pt $4f_{7/2}$ binding energy for Pt and 7 platinum alloys after reduction at 550°C in 5% H_2. The monometallic Pt sample had a Pt $4f_{7/2}$ binding energy of 70.9 eV and an asymmetric peak shape, consistent with metallic platinum. Similarly, the alloy samples also had asymmetric peak shapes, but the Pt $4f_{7/2}$ binding energy was shifted to higher binding energy. The core level shift for each alloy was calculated as the difference in Pt $4f_{7/2}$ binding energy between the alloy and the monometallic platinum. All of the alloys had a positive core level shift, which is consistent with platinum in the alloy being electronically modified. The varying magnitude of the core level

shifts for each alloy reflects the different electronic modification inherent to the heteroatomic bonds present in each phase.

S.2.4 Simulated particle dispersions

As RIXS is a bulk-sensitive technique, to simulate spectra in nanoparticle catalysts it was necessary to account for both surface and bulk metal contributions. For particles smaller than 9 nm, the fraction of surface atoms is at least 10% of the total metal content per particle, and for particles at the size scale in the present study (~1-3 nm) at least 30% of the total metal atoms are undercoordinated at the surface. Additionally, while the particle sizes for each catalyst is relatively consistent, sizes between different catalysts fluctuate, and as an approximate way to gauge the sensitivity of the spectra and electronic structure to changes in particle size, a range of dispersions were simulated from 30% – 60% (approximately 1.5 nm – 3 nm) as well as the limiting cases of 0% and 100% dispersion (a crystalline bulk and infinite surface, respectively).

S.2.5 Fractional charge and promoter strain comparisons

d-band centers shift depending on alloy identity, it is necessary to understand to what extent the fractional charge of platinum changes across the range of promoter metals. One measure of the charge transfer associated with alloy formation is the relative filling of Pt d-bands in the pure metal as compared to the alloy. A shift in either the total number of d electrons or relative filling of the d band would indicate charge transfer between Pt and promoter atoms. The total number of electrons across all 12 promoters has a MAE of 0.01 electrons (Supporting Information S.4.5), with a maximum deviation of 0.04 electrons relative to pure Pt for PtZn, which forms a (011) closest packed surface as compared to the 111 surface for pure Pt. The relative filling of the d-

band, expressed as the fraction of occupied Pt d electron states and total Pt d electron states, has a similar MAE of 0.02 electrons with a maximum deviation of 0.05 electrons (Supporting Information S.4.4). This indicates that despite the electronic interaction upon alloying observed qualitatively by the changing DOS among different promoters and shift in d-band center, there is no evidence of direct d-band charge transfer between Pt atoms and the promoter metals.

The relative size of the promoters (such as 4d post-transition metals In, and Sn) introduce strain on the Pt atoms, which change the adsorption and hence electronic properties[5–7]. By taking the strained lattice produced by alloying (a maximum +2.1% for Sn, and -3.1% for Fe) the changes in Pt d-states do not reproduce the splitting observed by alloying (Supporting Information S.3.5). Consequently, although strain has some influence the electronic properties of Pt, neither it nor charge transfer explain the observed splitting of Pt d-states upon alloy formation. We then are left with the conclusion that it is an interaction between Pt d-states and the promoter metal which maintains partial charge on each species that results in the observed splitting. While this splitting has been observed by others, in particular for Pd alloys[8], RIXS spectroscopy which probes valence states close to the Fermi energy provides additional insight into the observed d-DOS splitting.

S.2.6 RIXS peak identification

Difference RIXS plots are functions of the calculated Pt d-DOS, and we would like to compare the experimental and simulated RIXS spectra, to consequently relate shifts in the incident energy and energy transfer to the calculated electronic structure of Pt. To extract the location of the high energy peak, which would correspond to the highest intensity of emitted X-rays, a 2-D Gaussian

function is fitted to the RIXS map for each bimetallic, and then compared to pure Pt. This was calculated for each bimetallic alloy, and particle dispersion.

RIXS peaks are computationally identified by performing a 2-D Gaussian fitting scheme employed in Python with Numpy. Due to the broad, flat nature of many simulated high intensity peak, the 2-D fitting method would be more representative of the peak maxima. The difference in peak position for the Gaussian maximum versus absolute maximum is on the order of 0.1 eV – 0.2 eV due to the large peak width for many of the intermetallics. In the case of reduced core-hole broadening terms the Gaussian and absolute maxima locations were more strongly correlated. For the correlations with adsorption, where the core-hole broadening was normalized to 1, the absolute peak position was used as opposed to the Gaussian fit.

S.2.7 Alloy work functions

The absolute energy of the simulated high intensity peak is likely unreliable, as all simulated spectra are reference to the Fermi energy in vacuum, as opposed to measured spectra which are referenced to the core, but also the Fermi edge. From calculations in S.4.6, the work function of each alloy surface is similar to pure Pt, reflecting a consistent difference in between each alloy and the pure Pt reference state. A complete table of simulated incident energy and energy transfer maxima is provided in Supporting information S.4.7.

S.2.8 Error sources in RIXS energy transfer simulations

Energy transfer includes the relative energy change between the excitation from the core to unoccupied valence states compared to the decay from the occupied valence to the core. The energy transfer therefor relates to a relative change in the occupied and unoccupied states, as

opposed to the incident energy which measures the unoccupied states. The discrepancy between simulated and experimental RIXS is much larger, which may be attributed to the sensitivity in the relative shifts between unoccupied and occupied states with particle size. This could also reflect more experimental occupied states at lower energies than those modeling with DFT. The d-band becomes narrower for undercoordinated surface atoms, which manifests as a pronounced particle size effect for all promoters. The particle size effect for incident energies which correlate with the unoccupied states is smaller than the energy transfer term, which indicates that the size influences the range of occupied d-DOS states. This can be seen in the d-DOS of Figure 2, where the change in unoccupied peak position only weakly shifts with dispersion, as opposed to the spread in occupied states. While the trend in early transition metals is captured, there is a large deviation for the post-transition metals which results in a MAE of 0.41 eV. As the post-transition metals exhibit a tensile strain, it is possible that post-transition metal intermetallic nanoparticles have strain interactions which cannot be captured in a (111) slab model. This would be consistent with the particle size argument, as the incident energies are well-reproduced for the post-transition metals which could indicate a size or strain effect which shifts the occupied states and causes the slab model to under-estimate the energy transfer. Additionally, many of the Pt_3X alloy systems are stable over a compositional range, and small compositional changes or the presence of unalloyed platinum would lead to shifts in the experimental RIXS and XANES spectra.

S.2.9 Correlation of d band descriptors with RIXS spectra

From simulated RIXS spectra using Pt d-DOS which correlate to experimental measures of Pt valence orbitals in nanoparticle catalysts, correlations between features in RIXS spectra and features in the Pt d states would strengthen the chemical intuition of using the RIXS as a predictive

tool to designing alloy catalysts. While a correlation exists between the emission energy and *d*-band center (Supplementary Information S.3.7), the *d*-band center is the relative position of the total band center, including occupied and unoccupied states, to the Fermi energy. This does not directly include the splitting of Pt alloy states as observed in Figure 2. Additional augmentations of the d-band theory, such as including the width of the band, the kurtosis of the band, or the maximum of the Hilbert transform[8], do not significantly improve correlations (S.2.10). We can improve these correlations by considering the spectroscopy process itself as a basis for alternative descriptors. One observation is that RIXS spectra is a convolution of the product of occupied and unoccupied states. This strict separation of states lying above and below the Fermi energy provides intuition about how a model which includes the full span of possible *d*-states, both occupied and unoccupied, such as the *d*-band center would not capture the energy transfer changes or incident energy changes which rely on the convolution of separated electronic states.

Many descriptors have difficulties in systematically treating both late-transition and early-transition metals, and much work has been focused on treatment of the late transition metals such as the Hilbert transform maximum by Xin et al[8]. The accuracy of the RIXS convolution as a descriptor for adsorption in alloys can be understood through analogies with the original Newns-Anderson models for adsorption[9,10], where the strength of interaction is related to the coupling of metal electronic states projected onto adsorbates. Simplified *d* band descriptions correlate the interactions of the metal states to first order by their mean, and the relative shifts in band filling captures the relative alignment of metal and adsorbate bands to the Fermi energy. In comparing Pt atoms promoted by interaction with alloy metal atoms, the band centers are similar; however, the large degree of splitting is captured in part by the modified *d*-center including bandwidth We can contextualize the RIXS integral as including the convolution of occupied and unoccupied *d* states

relative to the Fermi energy, thus reminiscent of the full Newns-Anderson treatment where the distribution of occupied and unoccupied states includes higher order perturbations in the d-band. Therefore, the RIXS integral is an extension of the d-band theory which directly includes the relative distributions of the band, in the spirit of the Newns-Anderson theory.

The centers of states lying above and below the Fermi level can be related to the corresponding incident energy maximum and emission energy maximum, which was calculated by the general relation $\omega = \Omega - \Delta E$. In general, the maximum of the emission energy maximum shifts with the occupied d states as shown in Figure S.3.11. A similar analysis for incident energies and the center of unoccupied d states is provided in Figure S.3.11b with a similar average error as Figure S.3.11a. The correlation is strongest for smaller shifts in unoccupied states, below 0.4 eV relative to the Fermi energy, likely due to weaker interactions with occupied states in the integrand. The correlation is worse at high energies, where the unoccupied d center underestimates RIXS incident energies, which includes Zn, Ga, In. We propose that the RIXS energy transfer can be interpreted as being proportional to the difference between the unoccupied and occupied band center. This relation is shown in Figure S.3.11c, with a low MAE of 0.08 eV. There is some favorable error cancellation in the energy transfer relation, as the variance of the relative difference in unoccupied and occupied states is lower than each individual state (0.18 eV for Figure S.3.11a, and 0.15 eV for Figure S.3.11b). The range of bimetallics considered spans a range of 0 eV to 1 eV relative to pure Pt, and with a clear physical interpretation as the difference in the center of unoccupied and occupied d states. Discrepancies in these relationships may be due to coupling between occupied states which is implicit in the RIXS spectra and neglected in the band center analysis. Additionally, the core-hole lifetime of Pt (Γ) which was used as an experimental parameter in the RIXS equation, contributes to changes in the high intensity peak position.

S.2.10 Alternative *d*-band descriptors

To compare the RIXS energy transfer as a descriptor for unsaturated carbon adsorption, a suite of other potential descriptors were considered including the modified *d* descriptor by X, the center of unoccupied and occupied *d* states, the *d* band Kurtosis, and the *d* band skewness. The center of unoccupied and occupied states was calculated as the difference between the band center above and below the Fermi energy. The modified *d* descriptor was calculated as in[11] and is the center of the *d* band plus half the band width. The *d* band kurtosis was considered as another measure of alloy splitting and was calculated as the ratio of the 4th moment of the *d* band and the square of the 2th moment of the *d* band minus 3, the definition of excess kurtosis.[12] The skewness was calculated with the Fisher-Pearson equation, as the ratio of the third moment and the cube of the standard deviation[12]. A plot of these descriptors is provided in figure S.3.9. PtZn is excluded because of its 011 surface termination, as well as Pt_3In and Pt_3Sn which exert tensile strain.

MAEs for the set of promoters are higher for all considered alternate descriptors as compared to that reported in figure 5 of the main text. The MAE of the modified *d* band descriptor is 0.19 eV, with the largest deviation for Pt_3Ti. The splitting of unoccupied and occupied states have an MAE of 0.22 eV. The *d* band kurtosis has a MAE of 0.20 eV, and the skewness has a MAE of 0.25 eV. For reference, the MAE of the RIXS energy transfer is 0.10 eV. The maximum of the Hilbert transform as proposed by Xin, Vojvodic, and Norskov was used as well; however, this descriptor was only benchmarked for the late transition metals as discussed in the original paper, and does not scale with the early transition metals Ti and V.

S.2.11 Strain on adsorbates

The strain on Pt atoms induced by alloying or structural changes can influence the adsorption energies of intermediates. To examine whether differences in binding energies on alloys can be understood as Pt strain effects, the adsorption of carbon intermediates was considered by taking the relaxed alloy surface and replacing promoter atoms with Pt to produce a uniform Pt slab at the same strain as when alloyed. The results are summarized in Figure S.3.12 where dark circles represent the adsorption energy of unsaturated carbon intermediates at the most stable adsorption configuration. Red circles correspond to the adsorption of the same intermediate on a pure Pt slab (both surface and all subsurface layers) at the same strain, constructed by directly replacing promoter atoms with Pt. For all (111) alloy surfaces CH_3 was most stable at Pt top sites, CH_2 was most stable on Pt-Pt bridge sites, while CH and C were most stable in 3-fold Pt-Pt-Pt hollow sites. For Pt_3Ti and Pt_3V, CH2, CH, and C interacted strongly with the promoter metal causing adsorption to include the promoter metal as compared to the other promoters. For the PtZn (011) surface, CH_3 was most stable on Pt top sites, while CH_2, CH and C were most stable of Pt-Pt bridge sites. Representative adsorbate structures are shown in the Supporting Information S.3.8 The strain induced by the promoters had minimal effect on CH_2 and CH_3 adsorption, yet the binding energies of these intermediates with promoter metals change by nearly 0.7 eV for CH_2 indicating the strain effect on adsorption is small at these alloy compositions and identities.

Adsorption of the more unsaturated intermediates, CH and C, show a more pronounced stain effect, where the binding energy of C on strained pure Pt varies by just over 0.4 eV across the range of promoter metals and the binding energy of CH on strained pure Pt varies by nearly 0.2 eV. Despite a stronger strain effect, the range in C binding energies is over 1.4 eV and the range in CH binding energies is over 1.6 eV. As C and CH intermediates adsorb to 3-fold hollow sites, and therefore interact with 3 surface Pt atoms, the change in Pt-Pt distance more strongly

influences coordinative bonding with intermediates. A table of relevant Pt-C bond distances for different intermediates is provided in Supporting Information S.4.8. The binding energy of C and CH also do not seem to correlate with strain, indicating again that while strain effects do influence the adsorption of carbon intermediates, it does not explain neither the shape of Pt d-DOS nor trend in carbon adsorption energy. As discussed previously, the work functions of alloy surfaces and Pt surface Bader charges are nearly constant across the range of promoter metals, which cannot explain differences in adsorption between the intermediates. We therefor hypothesize that the predominant electronic effect of alloy formation is the splitting of occupied and unoccupied states observed in the Pt d-DOS of figure 1, and consequently the RIXS energy transfer observed from simulations and experiment.

S.2.12 CH_x scaling relationships for bimetallic surfaces

The binding energy of the set of unsaturated carbon intermediates including C, CH, CH_2, and CH_3 is correlated with the binding energy of atomic carbon in Figure S.3.13 as a scaling relationship. These scaling relationships, first derived by Pedersen et al[60], have been broadly applied to a wide range of catalysts to understand the behavior of chemically similar adsorbates[61–64]. From bond order conservation arguments, which define the slopes of scaling relationships, the slope of C/CH_3 is expected to be 0.25, for C/CH_2 is expected to be 0.50, and 0.75 for C/CH. Each relationship is regressed for the 3d metals, excluding Zn which forms a (011) surface termination. The 4d post-transition promoters, In and Sn, are excluded as they exert tensile strain as opposed to the other promoters. All three scaling relationships have MAEs less than 0.08 eV, likely due to a similar adsorbate structure. The slope of the C/CH_3 relationship is 0.24, as expected for bond order conservation. This is unsurprising as for all bimetallics CH_3 adsorbs to the top sites, and thus the coordination number is identical. The intercept is close to 0 eV, as all energies are referenced

to pure Pt. The slope of C/CH_2 is 0.26, not significantly different from C/CH_3 despite a predicted slope of 0.50. This is due, in part by the interactions of CH_2 intermediates with the oxophillic Ti and V promoters. Supporting Information S.3.10 includes the same scaling relationships where CH_2 is fixed in a configuration away from the promoter metals. In this case, the slope increases to 0.59 as both the C and CH_2 adsorbates are fixed to the same site. For C/CH, the slope is greater than the predicted value of 0.75. In fact, the predicted slope is close to 1, which would only occur if the number of bonds being formed to the surface for both C and CH were the same. This is unlikely, as atomic carbon binds strongly to the surface. Similar to CH_2, interactions of oxophilic promoters with the adsorbate states will shift the adsorption sites and change the location coordination for those promoters specifically. Even when constraining the position of CH and C adsorbates in S.3.10, the slope increases to 1.35, with a large intercept of -0.31 eV relative to platinum. The large slope and intercept indicate significantly different electronic interactions for C and CH among the different promoters which produces large deviations the predicted slopes and intercepts. Surface dipole interactions have been discussed by Choki, Majumdar and Greeley as causing deviations from bond order conservation[65]. Upon alloying, atomic carbon is forced away from an fcc hollow site to the 3-fold hollow site, which breaks the typical binding configuration of carbon in fcc metals.

S.3 Supplementary figures
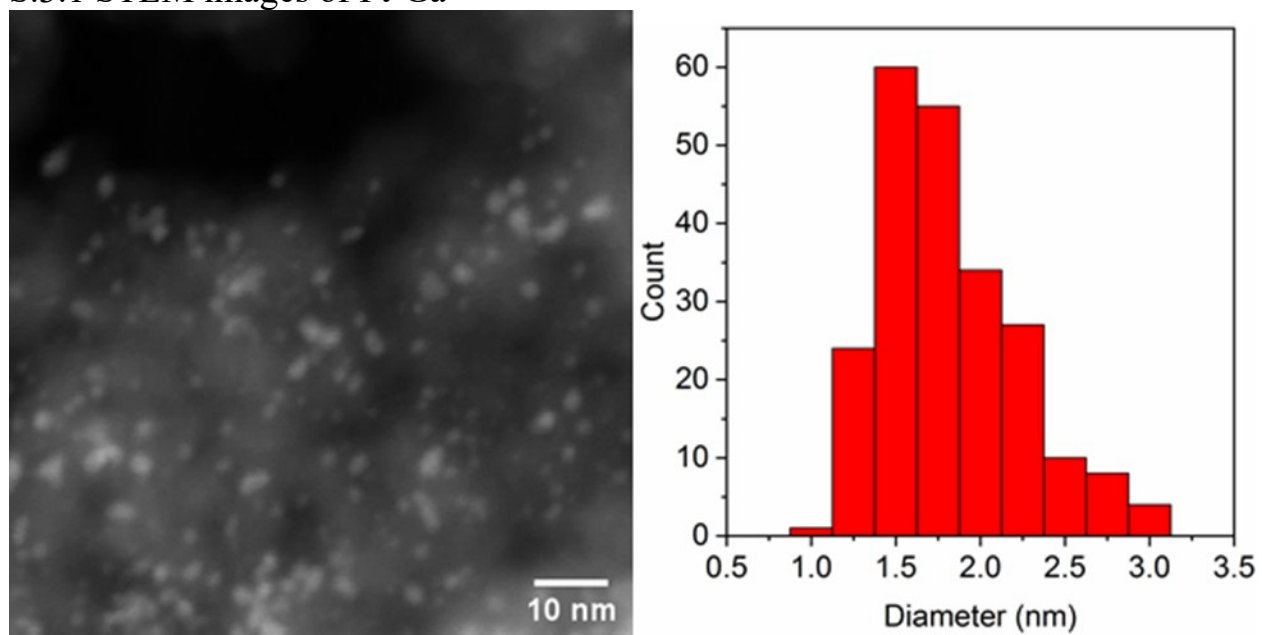
S.3.1 STEM images of Pt-Ga

Figure S.3.1: STEM image (left) and number average particle size distribution (right) of 5Pt-2.5Ga.
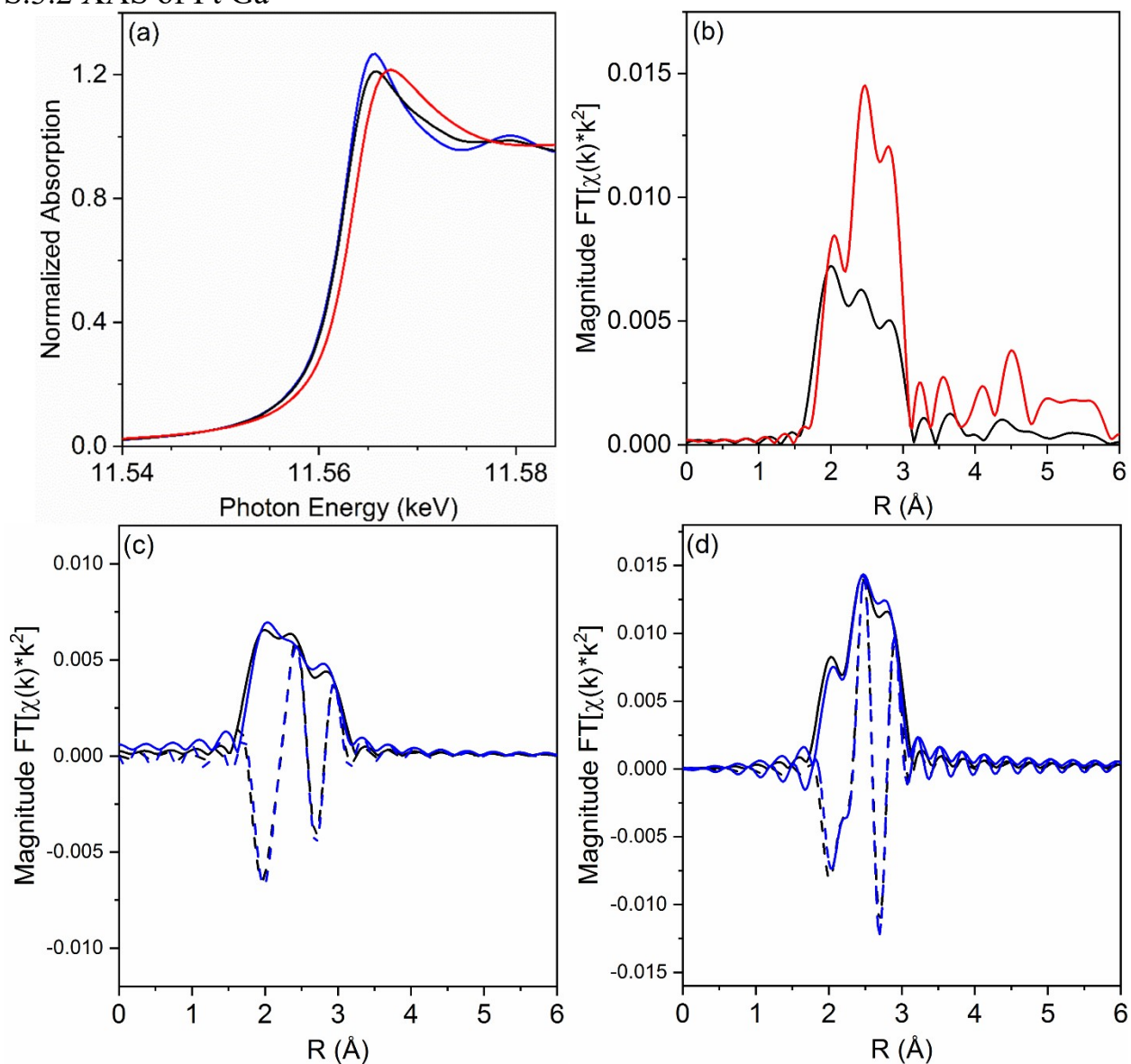
S.3.2 XAS of Pt Ga

Figure S.3.2: XANES and EXAFS results for Pt and Pt-Ga catalysts. (a) Pt L3 edge XANES for 3Pt (black) 5Pt-2.5Ga (red) and Pt foil (blue). (b) EXAFS of 3Pt (black) and 5Pt-2.5Ga (red). R space EXAFS fits of 5Pt-2.5Ga (c) and 3 Pt (d).
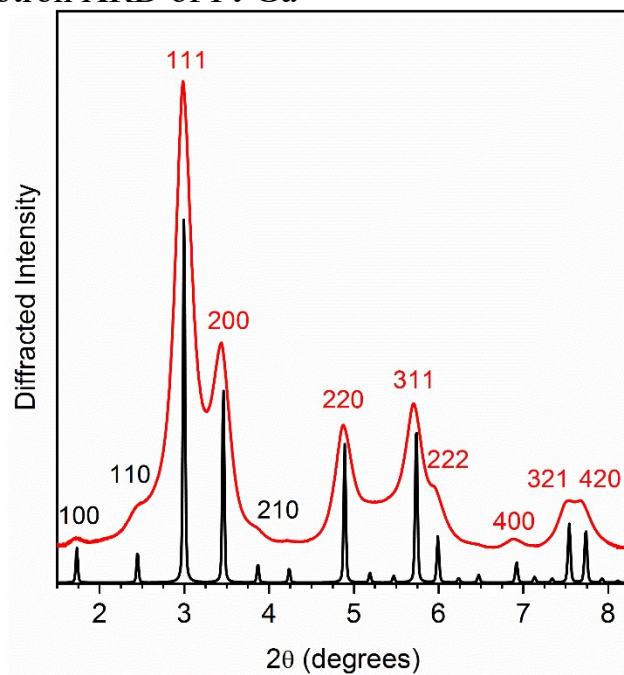
S.3.3 In-Situ synchrotron XRD of Pt-Ga

Figure S.3.3: In-situ synchrotron XRD pattern of 5Pt-2.5Ga (red) and Pt_3Ga standard simulation with a lattice parameter of 3.89 Å. Superlattice diffraction peaks are labeled in black and primary reflections are labeled in red.
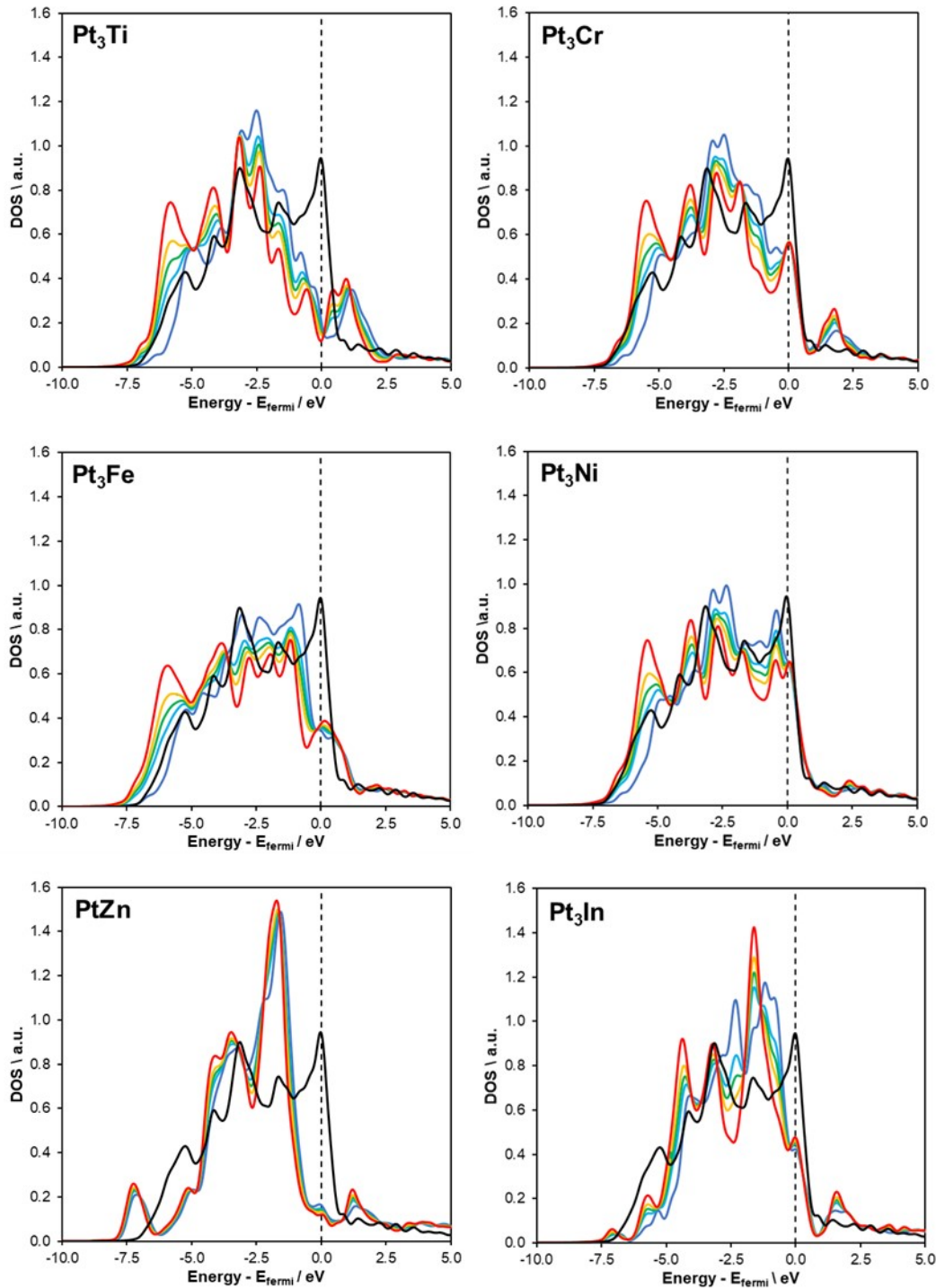
S.3.4 Intermetallic DOS

Figure S.3.4. Pt DOS remaining alloys not in Figure 1. The DOS are plotted for increasing dispersion from 0% (red), 30% (yellow), 45% (green), 60% (cyan), and 100% (blue).
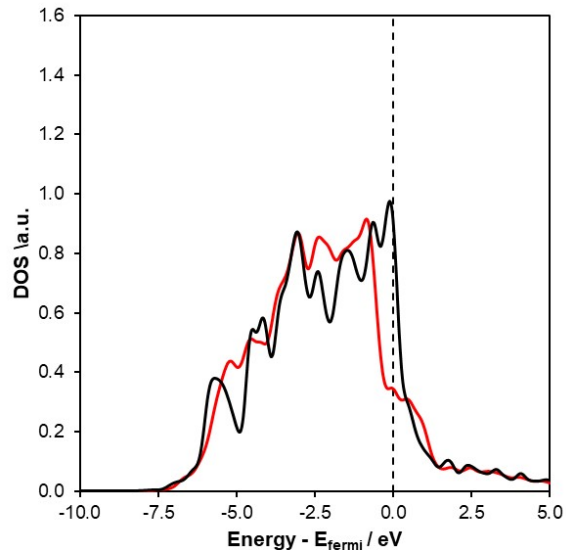
S.3.5 promoter strain effect on DOS

Figure S.3.5a. Pt d-DOS for Pt_3Fe (red) and pure Pt at the same lattice strain (-3.14%) as Pt_3Fe (black) for Pt surface atoms.
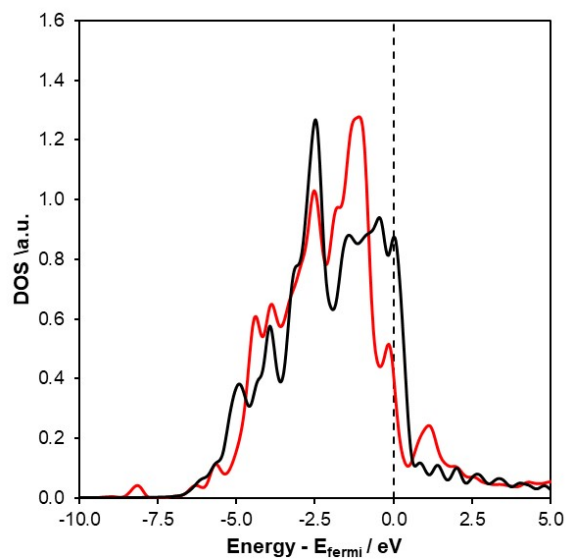

Figure S.3.5b. Pt d-DOS for Pt_3Sn (red) and pure Pt at the same lattice strain (+2.15%) as Pt_3Sn (black) for Pt surface atoms.
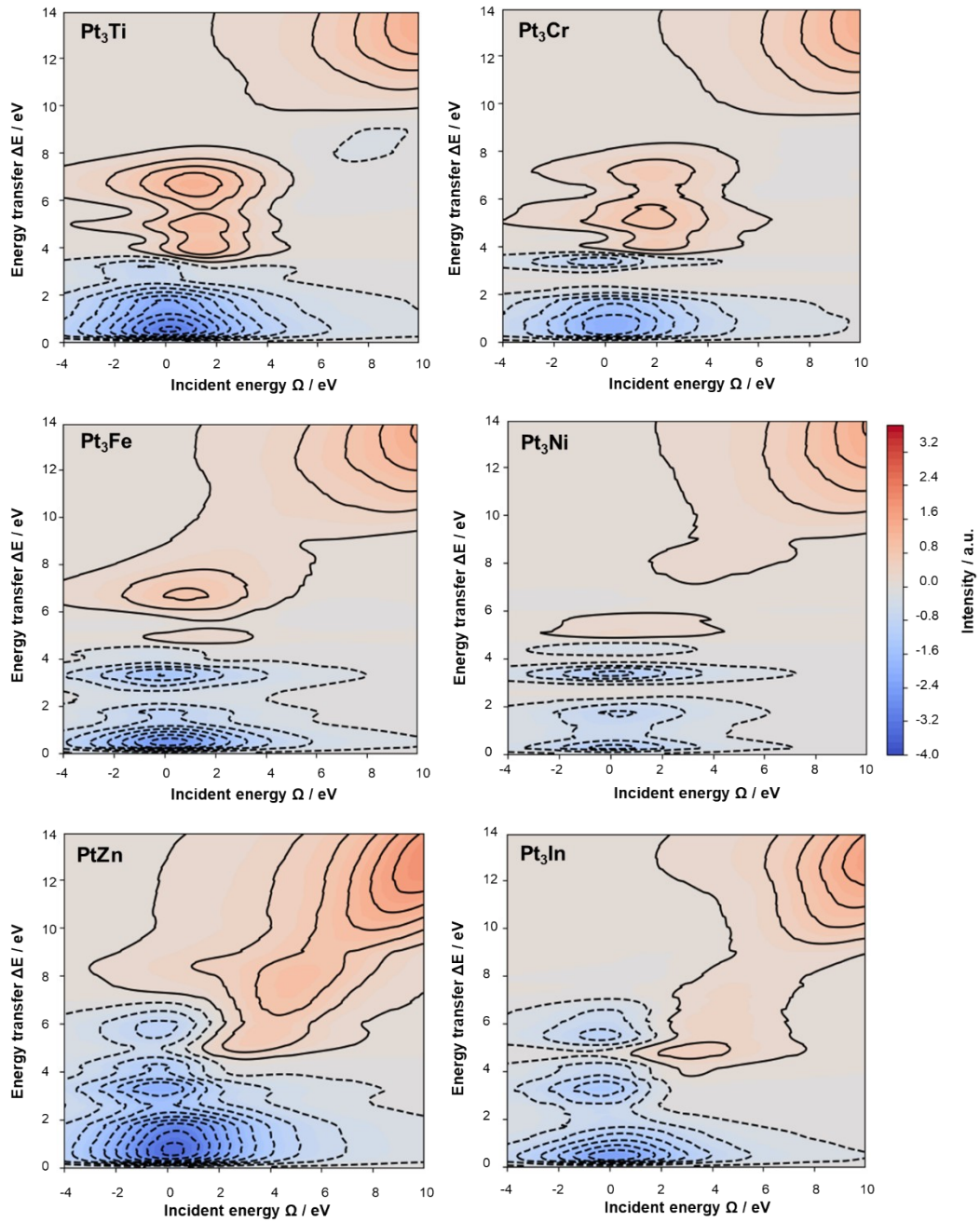
S.3.6 Simulated intermetallic RIXS

Figure S.3.6. Pt RIXS remaining alloys not in Figure 1.
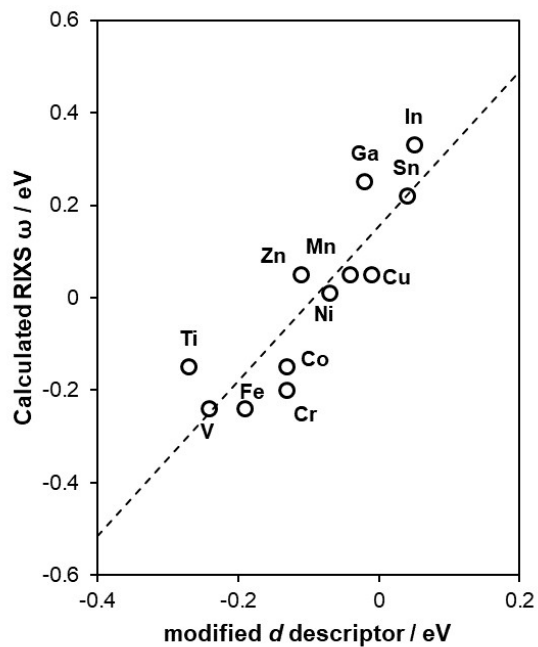
S.3.7 Modified *d* descriptor versus RIXS emission ω

Figure S.3.7. modified *d* descriptor including width, against RIXS emission energy which probes occupied *d* states.

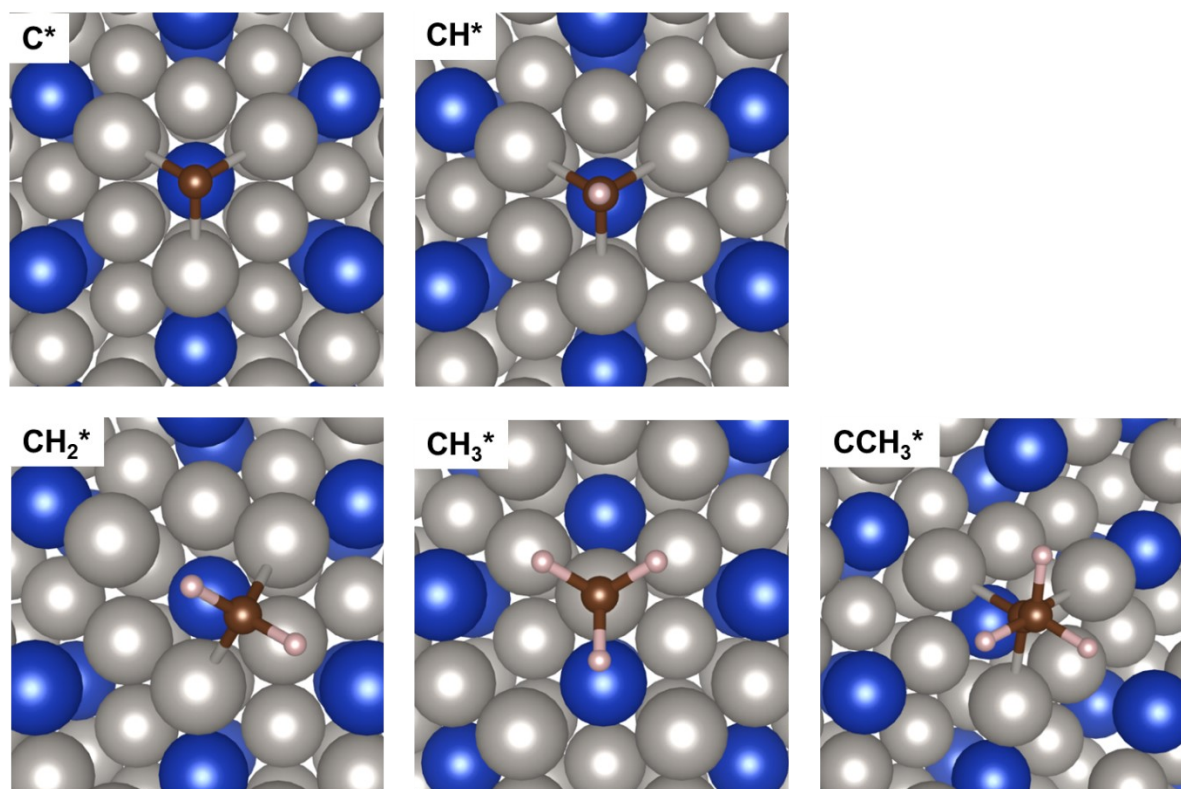## S.3.8 Representative adsorbate structures

Figure S.3.8a. Structures on (111) closest packed surfaces
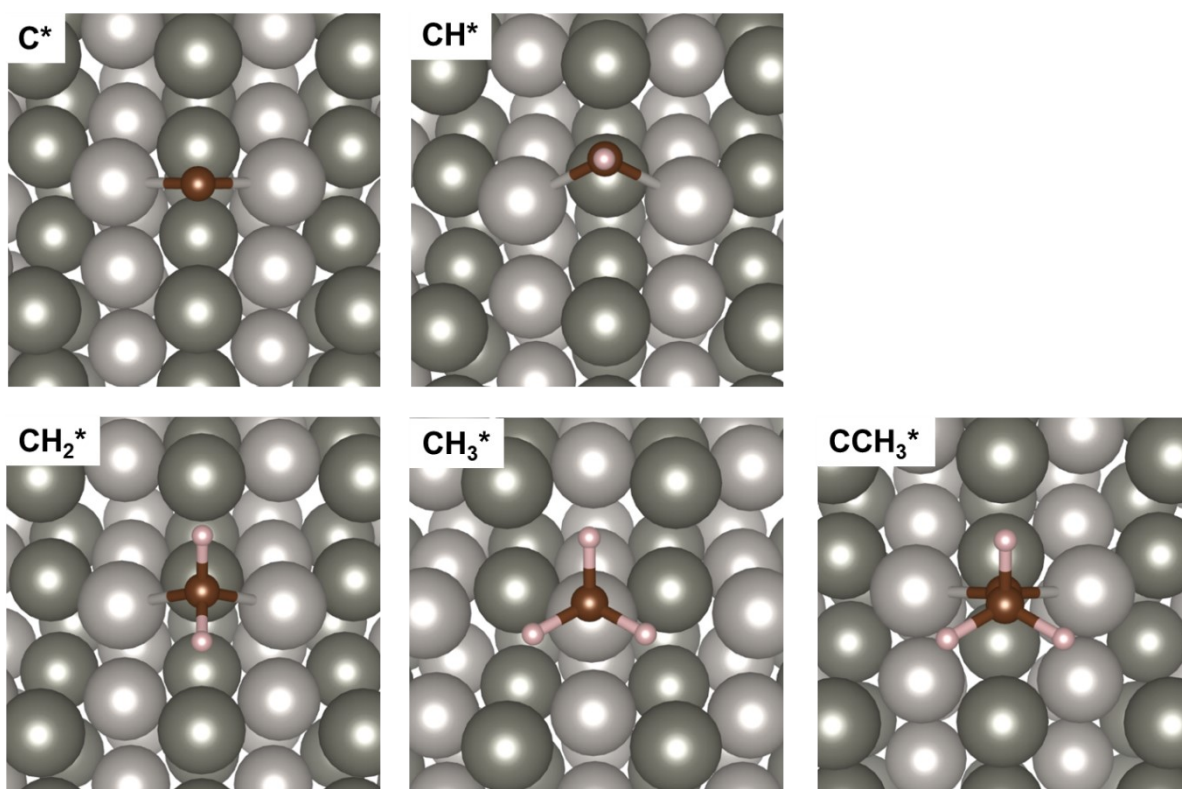
Figure S.3.8b. Structures on (011) PtZn closest packed surface

S.3.9 Comparison of alternative descriptors
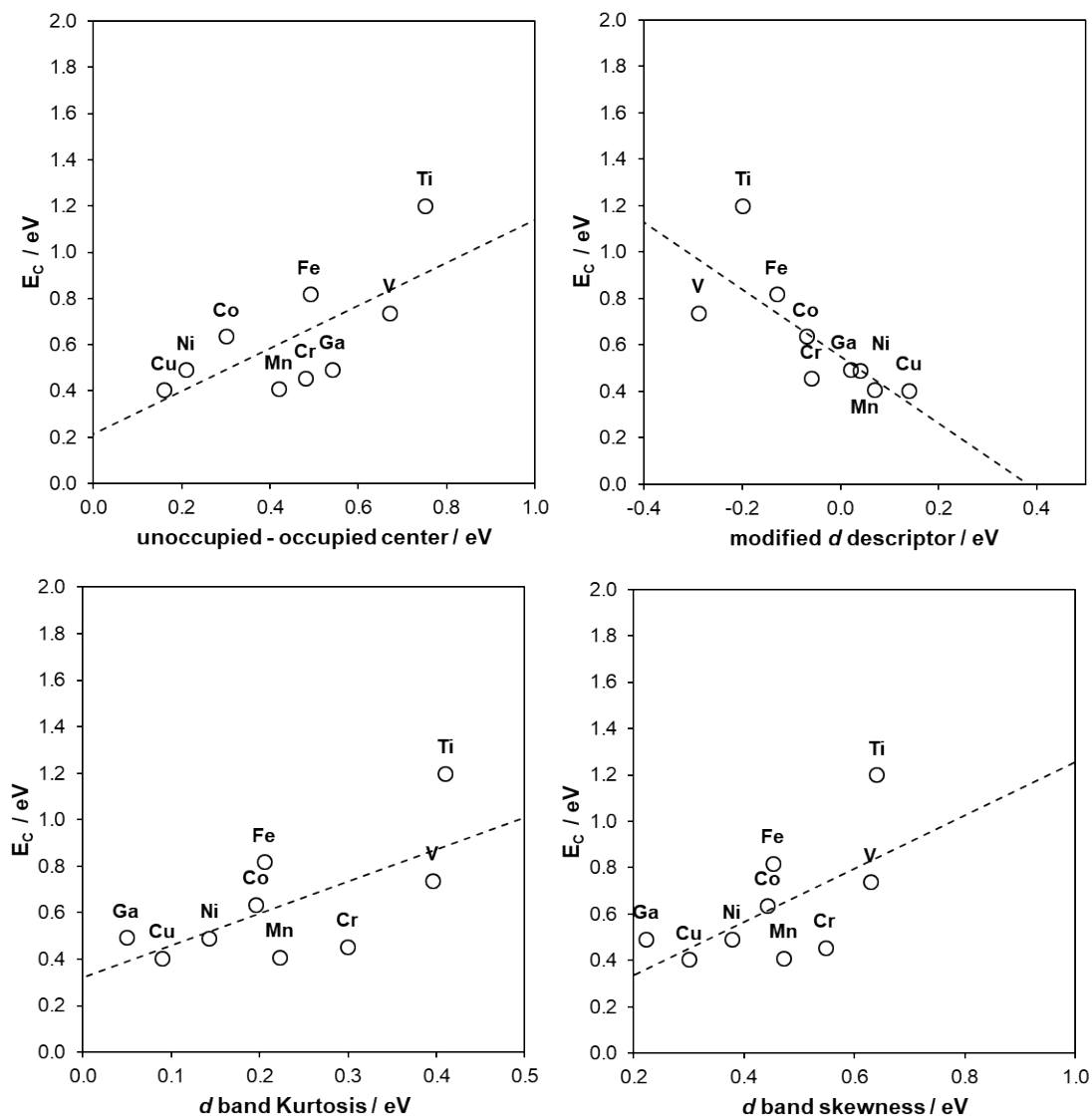
Figure S.3.9. Alternative descriptors considered against CH binding energy.

S.3.10 Fixed adsorption site correlations
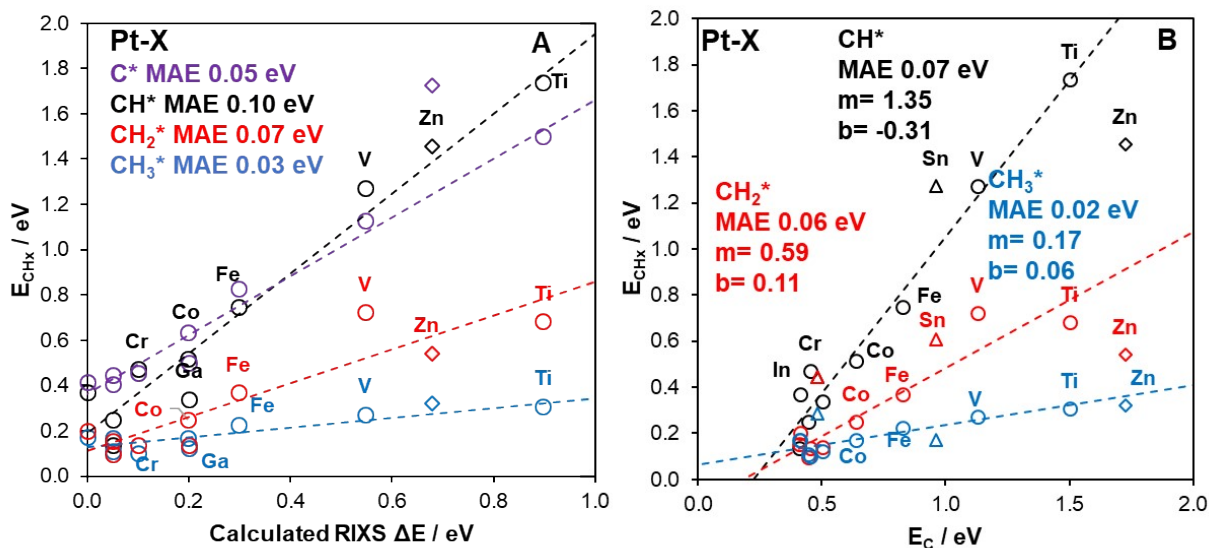
Figure S.3.10. RIXS energy transfer and scaling relationships where adsorbates on Pt_3V and Pt_3Ti have been fixed to not interact with the promoter metal.

S.3.11 RIXS correlations to *d* descriptors
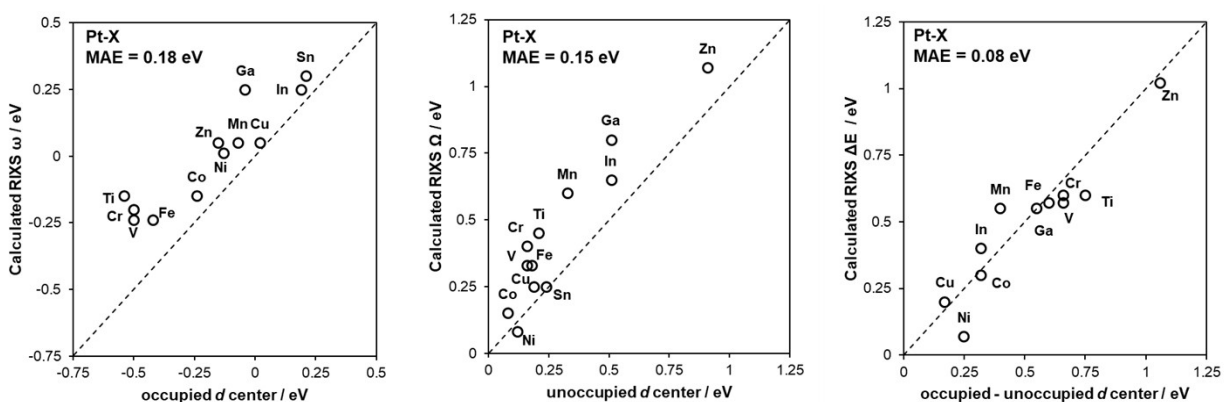
Figure S.3.11. Correlations between simulated RIXS spectral features and separated d-band descriptors across all bimetallic alloys in 2 nm particles. All quantities are reported relative to pure platinum.

S.3.12 Strain effects on adsorption
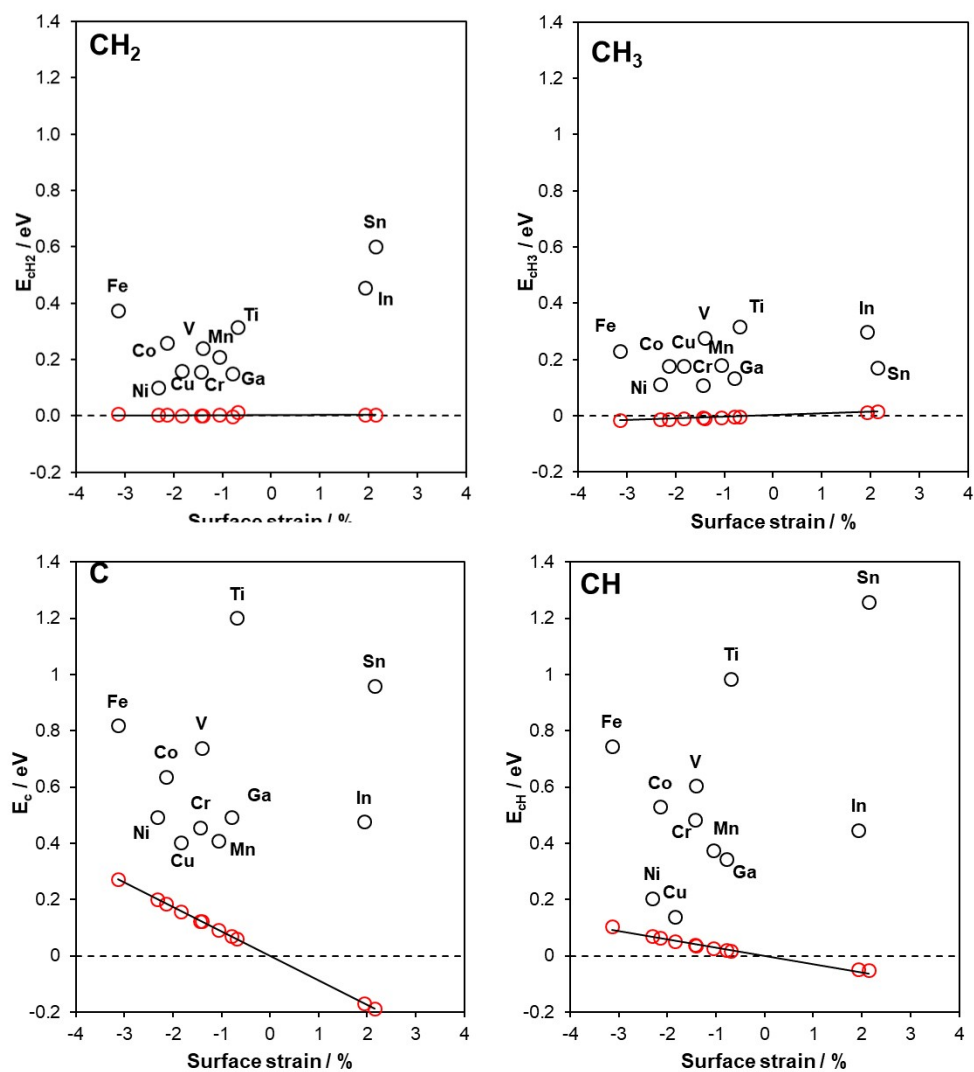
Figure S.3.12. Adsorption of unsaturated methyl intermediates on alloy (black circles) and strained Pt surfaces (red circles) plotted against the surface strain. The origin corresponds to adsorption on an unstrained pure Pt surface.

S.3.13 Bimetallic Scaling Relationships

Figure S.3.13. Scaling relationships for molecular adsorbates on transition metal surfaces. Note Pt3Sn and Pt3In are 4d metals, and PtZn is a 1:1 composition with a (011) surface termination and are excluded from the scaling relationship.
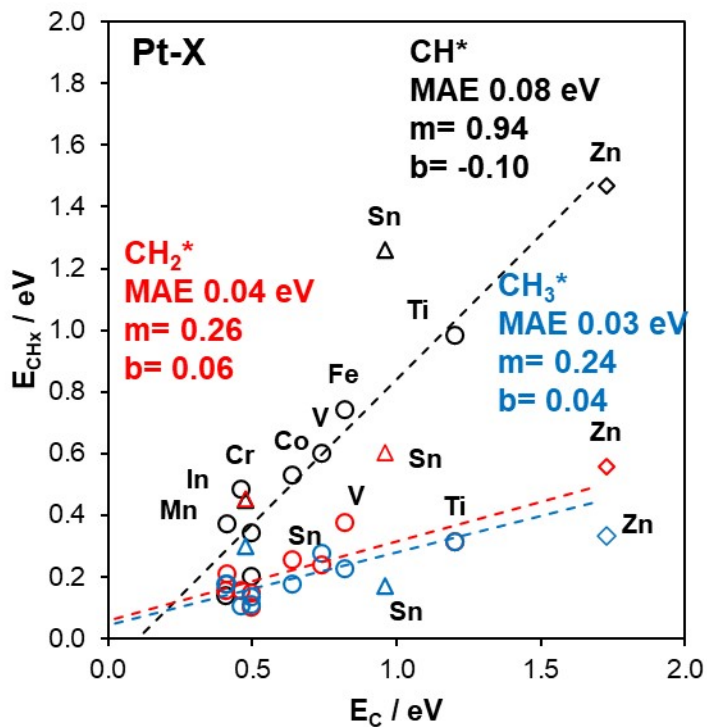
S.3.14 CH-CCH3 scaling relationship
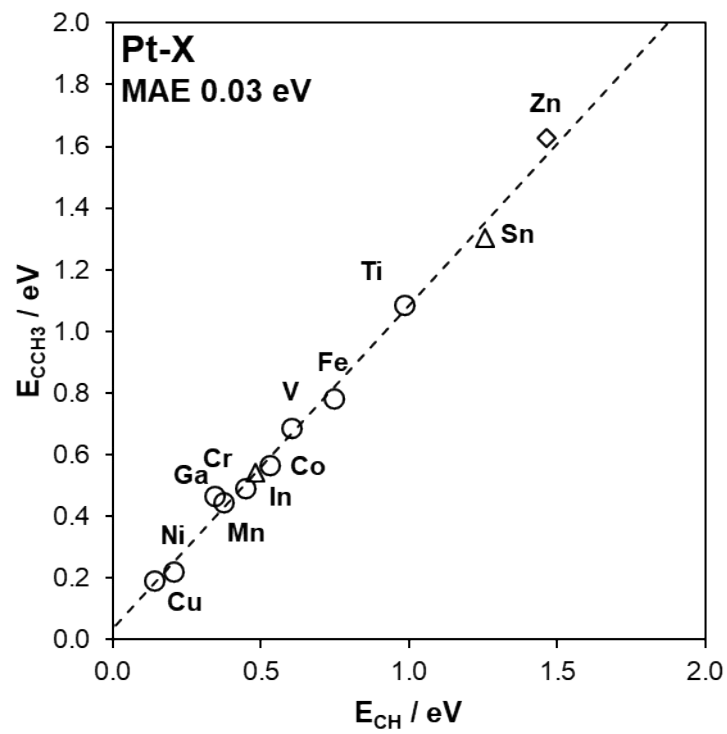
Figure S.3.14. Scaling relationship for adsorption of CH and CCH3.

S.4 Supplementary tables
S.4.1 Pt L3 edge EXAFS fitting parameters for Pt and Pt-Ga

Sample	XANES edge energy (eV)	Path	CN	R (Å)	DWF (Å^2)	E$_0$ (eV)
Pt foil	11562.8	Pt-Pt	12	2.77	0	0
3Pt	11562.8	Pt-Pt	8.8	2.74	0.002	-0.8
5Pt-2.5Ga	11563.6	Pt-Pt	5.7	2.75	0.003	-3.8
		Pt-Ga	2.5	2.50	0.006	-7.5

S.4.2 Pt 4f XPS core level shifts for platinum alloys

Sample	Pt $4f_{7/2}$ binding energy (eV)	Pt $4f_{7/2}$ FWHM (eV)	Pt 4f spin orbital splitting (eV)	Core level shift (eV)
Pt	70.9	2.0	3.4	-
Pt$_3$V	71.3	2.2	3.5	0.4
Pt$_3$Mn	71.0	1.7	3.3	0.1
Pt$_3$Fe	71.4	2.0	3.4	0.5
Pt$_3$Co	71.5	2.1	3.4	0.6
Pt$_3$Ga	71.6	1.9	3.4	0.7
Pt$_3$In	71.3	1.9	3.3	0.4
PtZn	71.7	1.9	3.3	0.8

S.4.3 intermetallic lattice constants

Intermetallic phase	Lattice constant / Å
Pt_3Ti	3.949
Pt_3V	3.921
Pt_3Cr	3.920
Pt_3Mn	3.935
Pt_3Fe	3.852
Pt_3Co	3.892
Pt_3Ni	3.885
Pt_3Cu	3.904
PtZn[a]	a=2.885, c=3.528
Pt_3Ga	3.945
Pt_3In	4.054
Pt_3Sn	4.062
Pt[b]	3.977

[a]PtZn has a tetragonal unit cell structure, as oppose to others forming a fcc structure.
[b]Pure Pt reference lattice

S.4.4 integrated *d*-state filling

Intermetallic phase[a]	Total Pt *d* electron count[b]	Fractional Pt *d* band filling[c]
Pt$_3$Ti	4.45	0.87
Pt$_3$V	4.44	0.86
Pt$_3$Cr	4.43	0.86
Pt$_3$Mn	4.41	0.87
Pt$_3$Fe	4.43	0.87
Pt$_3$Co	4.42	0.86
Pt$_3$Ni	4.42	0.86
Pt$_3$Cu	4.41	0.87
PtZn	4.38	0.89
Pt$_3$Ga	4.42	0.88
Pt$_3$In	4.41	0.88
Pt$_3$Sn	4.41	0.87
Pt[d]	4.43	0.86

[a]the DOS corresponding to 45% dispersion was used for each intermetallic alloy
[b]evaluated as the average of spin up and spin down across each surface Pt atom
[c]Integral of states below the Fermi energy divided by the total *d* states up to the cutoff of +5 eV
[d]Pure Pt reference lattice

S.4.5 Alloy Bader charges

Intermetallic phase[a]	Pt Bader charge / e
Pt_3Ti	0.46
Pt_3V	0.40
Pt_3Cr	0.33
Pt_3Mn	0.32
Pt_3Fe	0.27
Pt_3Co	0.20
Pt_3Ni	0.14
Pt_3Cu	0.14
PtZn	0.57
Pt_3Ga	0.25
Pt_3In	0.26
Pt_3Sn	0.32
Pt[b]	0.05

[a]Only surface Pt atoms were considered
[b]Pure Pt reference lattice

S.4.6 Alloy work functions

Intermetallic phase	Work function[a] / eV
Pt_3Ti	5.19
Pt_3V	5.23
Pt_3Cr	5.23
Pt_3Mn	5.18
Pt_3Fe	5.36
Pt_3Co	5.36
Pt_3Ni	5.46
Pt_3Cu	5.38
PtZn	4.96
Pt_3Ga	5.07
Pt_3In	4.94
Pt_3Sn	5.18
Pt[c]	5.68

[a]Calculated as the electrostatic potential of the slab vacuum φ relative to the Fermi energy. All vacuum potentials were flat across the vacuum.

S.4.7 Calculated RIXS Peak Positions

Intermetallic phase[a]	Incident energy maximum Ω / eV	Energy transfer maximum ΔE / eV
Pt_3Ti	0.45	0.60
Pt_3V	0.33	0.57
Pt_3Cr	0.40	0.60
Pt_3Mn	0.60	0.55
Pt_3Fe	0.33	0.57
Pt_3Co	0.15	0.30
Pt_3Ni	0.08	0.07
Pt_3Cu	0.25	0.20
$PtZn$	1.07	1.02
Pt_3Ga	0.80	0.55
Pt_3In	0.65	0.40
Pt_3Sn	0.25	-0.05

[a]Reported values are for 45% dispersion

S.4.8 Adsorbate CH bond distances

Intermetallic phase	Pt-C distances / Å	Pt-C(H) distances / Å	Pt-C(H$_2$) distances / Å	Pt-C(H$_3$) distances / Å	Pt-C(CH$_3$) distances / Å
Pt$_3$Ti	1.96	2.08	2.12	2.11	2.05
Pt$_3$V	1.98	2.08	2.12	2.10	2.03
Pt$_3$Cr	1.96	2.01	2.07	2.10	2.02
Pt$_3$Mn	1.96	2.01	2.06	2.10	2.02
Pt$_3$Fe	1.96	2.00	2.06	2.09	2.02
Pt$_3$Co	1.95	2.01	2.06	2.09	2.02
Pt$_3$Ni	1.94	2.00	2.05	2.08	2.02
Pt$_3$Cu	1.94	2.00	2.04	2.08	2.02
PtZn	1.90	2.02	2.10	2.12	1.97
Pt$_3$Ga	1.97	2.00	2.05	2.10	2.01
Pt$_3$In	1.96	2.01	2.06	2.10	2.02
Pt$_3$Sn	1.98	2.01	2.05	2.10	2.03
Pt[c]	1.92	2.01	2.05	2.07	2.03

S.5 Supplementary References

[1] J. Schindelin, I. Arganda-Carreras, E. Frise, V. Kaynig, M. Longair, T. Pietzsch, S. Preibisch, C. Rueden, S. Saalfeld, B. Schmid, J.-Y. Tinevez, D. J. White, V. Hartenstein, K. Eliceiri, P. Tomancak, A. Cardona, *Nature Methods* **2012**, *9*, 676–682.

[2] A. P. Hammersley, *Grenoble, France: European Synchrotron Radiation Source* **1997**.

[3] A. P. Hammersley, S. O. Svensson, M. Hanfland, A. N. Fitch, D. Hausermann, *High Pressure Research* **1996**, *14*, 235–248.

[4] S. Bhan, K. Schubert, *ZEITSCHRIFT FUR METALLKUNDE* **1960**, *51*, 327–339.

[5] P. Strasser, S. Koh, T. Anniyev, J. Greeley, K. More, C. Yu, Z. Liu, S. Kaya, D. Nordlund, H. Ogasawara, M. F. Toney, A. Nilsson, *Nature Chemistry* **2010**, *2*, 454–460.

[6] J. Greeley, W. P. Krekelberg, M. Mavrikakis, *Angewandte Chemie* **2004**, *116*, 4396–4400.

[7] F. Abild-Pedersen, J. Greeley, J. K. Nørskov, *Catal Lett* **2005**, *105*, 9–13.

[8] H. Xin, A. Vojvodic, J. Voss, J. K. Nørskov, F. Abild-Pedersen, *Phys. Rev. B* **2014**, *89*, 115114.

[9] D. M. Newns, *Physical Review* **1969**, *178*, 1123–1135.

[10] P. W. Anderson, *Physical Review* **1961**, *124*, 41–53.

[11] A. Vojvodic, J. K. Nørskov, F. Abild-Pedersen, *Top Catal* **2014**, *57*, 25–32.

[12] "NIST/SEMATECH e-Handbook of Statistical Methods," can be found under https://www.itl.nist.gov/div898/handbook/index.htm, **n.d.**